AGU PUBLICATIONS

JGR

Journal of Geophysical Research: Space Physics

RESEARCH ARTICLE
10.1002/2016JA023269

Special Section:
Measurement Techniques in Solar and Space Physics: Particles

Electrostatic analyzer design for solar wind proton measurements with high temporal, energy, and angular resolutions

Antoine Cara[1,2], Benoit Lavraud[1,2], Andrei Fedorov[1,2], Johan De Keyser[3], Rossana DeMarco[4], M. Federica Marcucci[4], Francesco Valentini[5], Sergio Servidio[5], and Roberto Bruno[4]

[1]Institut de Recherche en Astrophysique et Planétologie, Université de Toulouse, Toulouse, France, [2]Centre National de la Recherche Scientifique, Toulouse, France, [3]BIRA-IASB, Brussels, Belgium, [4]IAPS INAF, Rome, Italy, [5]Dipartimento di Fisica, Università della Calabria, Rende (CS), Italy

Key Points:
- A new solar wind ion instrument design is presented
- Simulations are used to define a design with unprecedented temporal and angular resolutions
- A plasma turbulence simulation is used to show the measurement capabilities achieved

Correspondence to:
A. Cara,
Antoine.Cara@irap.omp.eu

Citation:
Cara, A., B. Lavraud, A. Fedorov, J. De Keyser, R. DeMarco, M. F. Marcucci, F. Valentini, S. Servidio, and R. Bruno (2017), Electrostatic analyzer design for solar wind proton measurements with high temporal, energy, and angular resolutions, *J. Geophys. Res. Space Physics*, *122*, 1439–1450, doi:10.1002/2016JA023269.

Received 2 AUG 2016
Accepted 17 JAN 2017
Accepted article online 20 JAN 2017
Published online 6 FEB 2017

Abstract We present the design study of an electrostatic analyzer that permits combined high temporal, energy, and angular resolution measurements of solar wind ions. The requirements for high temporal, energy, and angular resolutions, combined with the need for sufficient counting statistics, lead to an electrostatic analyzer with large radius (140 mm) and large geometric factor. The resulting high count rates require the use of channel electron multipliers (CEMs), instead of microchannel plates, to avoid saturation. The large radius further permits the placement of 32 CEM detectors at the analyzer focal plane, thereby providing very high angular resolution in azimuth (1.5°). Electrostatic simulations were performed to define the analyzer geometric factor, energy resolution, analyzer constant (K), elevation response, etc. Simulations were also performed to define the geometry of the deflectors and collimator that are used to provide the proper energy resolution, field of view, and angular resolution (1.5°) in elevation as well (the total field of view of the design is ±24° × ±24°). We show how this design permits unprecedented measurements of the fine structure of the solar wind proton beam and other important features such as temperature anisotropy. This design is used for the Cold Solar Wind instrument of the medium-class Turbulent Heating ObserveR mission, currently in phase A at the European Space Agency. These unprecedented measurement capabilities are in accordance with and even beyond the requirements of the mission.

1. Introduction

1.1. Upcoming Missions and Science Objectives

Current space missions such as Wind [*Lin et al*., 1995], ACE [*McComas et al*., 1998], or Cluster [*Rème et al*., 2001] typically perform in situ ion measurements in space with rather low temporal (few seconds at best) and angular resolutions (~3° at best). While such properties are sufficient for numerous purposes, they are far from being sufficient for the study of kinetic-scale processes associated with turbulence, shocks, and reconnection, in particular in the solar wind [e.g., *Schwartz et al*., 2009; *Bruno and Carbone*, 2013]. The requirement for high energy and angular resolutions comes, on the one hand, from the basic property of solar wind proton distribution functions that have the form of a cold beam with only a small angular width. Typically, it can be described by a drifting bi-Maxwellian (with a noticeable temperature anisotropy), but it often manifests more complex shapes [e.g., *Bruno and Carbone*, 2013]. Such non-Maxwellian features indicate the presence of fundamental kinetic plasma instabilities that, together with turbulence, are crucial for understanding the dynamics of the interplanetary medium [e.g., *Marsch*, 2006]. The requirement for high time resolution comes, on the other hand, from the fact that (1) the solar wind flows very fast past the spacecraft, leaving little time to sample solar wind structures such as thin current sheets, and (2) that the typical growth time of ion instabilities in the solar wind is on the order of few cyclotron periods [*Montgomery et al*., 1975]. A good understanding of wave-particle interactions can thus only be obtained if the growing phase of instability is observed; i.e., several observations of the full 3-D velocity distribution function are required during the development of the instability itself.

Solar wind ion measurements are currently being performed, for example, by Cluster [*Rème et al*., 2001], ACE [*McComas et al*., 1998], and Wind [*Ogilvie et al*., 1995]. Such measurements will be performed with enhanced capabilities on future missions such as Solar Orbiter (Proton and Alpha Sensor; PAS) and Solar Probe Plus (Solar Probe Analyzer; SPAN [*Kasper et al*., 2016]). The properties of these instruments are shown in Table 1.

Table 1. Main Properties of a Few Past and Future Solar Wind Instruments (for Full Distribution Function Measurement)[a]

	Cluster (HIA)	Solar Orbiter (PAS)	Solar Probe Plus (SPAN)	THOR (CSW)
Type of instrument	ESA + MCP	Deflector + ESA + CEM	Deflector + ESA + MCP + TOF	Deflector + ESA + CEM
Spacecraft spin and FOV	15 rpm Spin axis orthogonal to FOV	3 axis stabilized	3 axis stabilized	2 rpm Spin axis aligned with FOV
3-D sampling time resolution	4 s	1 s	3.5 s	150 ms
Full energy range	5 eV–32 keV	200 eV–20 keV	5 eV–30 keV	200 eV–20 keV (20 eV–20 keV)
Energy resolution $\Delta E/E$	18%	~7%	7%	5%–8% (7%)
Azimuth resolution	5.6°	6°	11.25°	3° (1.5°)
Elevation resolution	5.6°	5°	5°	3° (1.5°)
Azimuth range	360°	−24° + 42°	240°	±24°
Elevation range	±180°	±22.5°	±60°	±24°
Sphere radius	40.2 mm	72.5 mm	~35 mm	140 mm
Geometric factor (total) [$cm^2 \cdot sr \cdot keV/keV$]	$1.9 \cdot 10^{-4}$ (one half) $4.9 \cdot 10^{-3}$ (other half)	$4.4 \cdot 10^{-5}$ (11 anodes)	Not known	$7 \cdot 10^{-4}$ (32 anodes)

[a]TOF: time of flight.

However, as presented here and in the companion paper [*DeMarco et al*., 2016], the study of kinetic-scale processes in the solar wind (turbulence, etc.) requires much more detailed measurements of the solar wind proton distribution function. Note also that despite a high time resolution (150 ms), the ion instrument Magnetospheric Multiscale (MMS) [*Pollock et al*., 2016] mission is not designed for fine measurements of the proton beam in the solar wind, owing to an 11.25° angular resolution.

The THOR (Turbulent Heating ObserveR) mission [*Vaivads et al*., 2016] (http://thor.irfu.se/), which is currently in phase A as a medium-class M4 mission within the science program of the European Space Agency, is designed to address turbulent energy dissipation and particle energization in the interplanetary plasma, in different physical regimes and different regions (Earth's bow shock and magnetosheath, foreshock, undisturbed solar wind, and interplanetary shocks). To maximize the time spent in the key target regions, the THOR orbit is close to the ecliptic plane with three science phases. Each phase has a different orbit and a term of 1 year. The first year is dedicated to magnetosheath and bow shock studies with an apogee of 16 R_E (Earth radii). The second phase targets the solar wind, shock, and foreshock with an apogee of 26 R_E. The third phase will focus on the pristine solar wind and interplanetary shocks with an apogee of 60 R_E. Here we present the work that has been performed to design the Cold Solar Wind (CSW) instrument of the THOR mission, which is dedicated to the measurement of the solar wind proton beam with unprecedented temporal (150 ms) and angular (1.5°) resolutions. CSW will measure the three-dimensional distribution function of solar wind ions in the range of 20 eV–20 keV. In certain modes with a large energy range it will also measure alphas. To ensure high temporal resolution and continuous measurements of the solar wind ion beam, the CSW instrument is accommodated on the side of the spacecraft with a field of view centered on the Sun direction and aligned with the spacecraft spin axis. Moreover, the high angular resolution (down to 1.5°) requires a slow spacecraft spin rate (2 rpm is planned for the THOR spacecraft).

Table 1 lists the basic properties of some solar wind instruments in comparison to the properties of the design reported here for CSW on THOR. The values given for CSW in the table are the measurement requirements that ensue from the science requirements of the mission (http://thor.irfu.se/). Between parentheses we give the actual characteristics planned for the CSW instrument on the basis of the present study. The proposed increase in angular resolution in particular will strongly benefit the science return of the mission as shown in section 3 and in the *DeMarco et al*. [2016].

1.2. Basic Instrument Design

The designs most frequently used for solar wind ion measurements are based on Faraday cups or electrostatic analyzers (ESAs) coupled with detectors. Faraday cups are composed of a cup with grids and two semicircular collector plates. The grids are polarized to select incident particles by energy (as a retarding potential analyzer), and the particle flux is estimated through the measurement of the current on each collector. ESAs select incident particles by deflecting them with an electrostatic field applied between concentric plates.

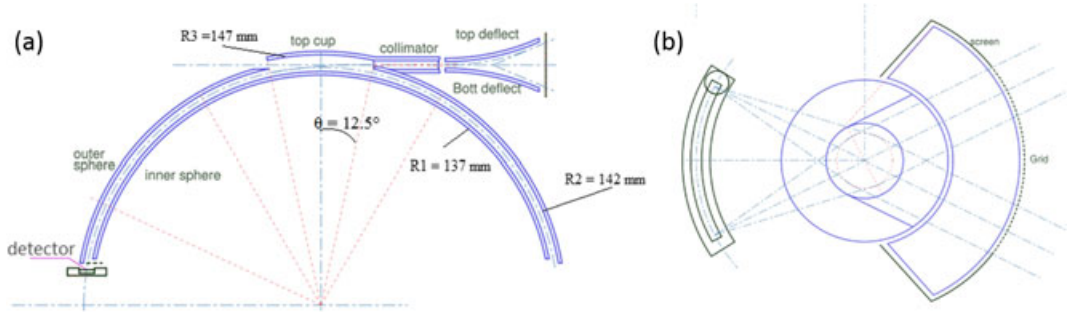

Figure 1. Two-dimensional schematics of (a) analyzer electrostatic design and (b) typical top-hat focusing properties.

Only particles within the appropriate energy range are able to reach detectors placed at the exit of the analyzer (channel electron multipliers or microchannel plates). ESAs are often coupled with deflector systems at their entrance in order to measure out of the natural analyzer detection plane. All these aspects are further detailed in the next sections.

The spectrometer used for CSW is based on a top-hat electrostatic analyzer design [*Carlson et al.*, 1982], which is composed of two concentric hemispheric plates for ion energy-per-charge selection. Such a design permits fine focusing onto the detectors at the ESA exit, in accordance with the requirement for high angular resolution measurements (Figure 1b). The outer hemisphere potential is set to ground, while the inner sphere potential varies according to the particle energy-per-charge to measure (Figure 1a). The elevation angle selection is performed, thanks to high voltages applied on deflector plates at the entrance of the analyzer which allows a fast 3-D measurement (e.g., Solar Orbiter or Solar Probe Plus; Table 1). A collimator is used between the deflectors and the top-hat entrance to ensure the required energy and angular (in elevation) resolutions, while the azimuthal resolution (Figure 1b) is obtained through appropriate sectorization of the detectors and anodes.

In section 2, we present the design of the electrostatic optics and detectors, focusing first on the ESA and collimator that will define the energy, elevation, and azimuth response of the instrument. The study then focuses on the design of the deflectors. The final design performance characteristics are presented in section 3.

2. Electrostatic Optic Design

2.1. Electrostatic Analyzer

In this section, the ESA and collimator are only considered to characterize the energy, elevation, and azimuth response that correspond to the needs of the instrument.

2.1.1. Geometric Design

As mentioned in Table 1, the baseline 3-D ion distribution sampling time for THOR/CSW is 150 ms. Yet the accumulated counts per elementary 3-D distribution bin must be high enough to ensure sufficient statistical significance of the data, as further addressed in section 3. The requirement for high counting statistics, combined with the required high time resolution, means that the detectors used at the ESA exit must have a high count rate saturation threshold.

MCP (microchannel plate) detectors typically saturate at 1,000,000 c s^{-1} cm^{-2}. Basic calculations show that for an electrostatic analyzer of radius 14 cm with an energy resolution of 7% (the basic properties of the instrument as determined through the analysis performed in the next sections), MCPs with an anode size of 3° would lead to saturation for any counting statistics above 500 counts in a baseline 1 ms elementary accumulation time. What this basic calculation shows is that MCPs are not appropriate for such high count rate requirements. The baseline design thus uses channel electron multipliers (CEMs) instead of MCPs as detectors. The advantages are twofold: (1) CEM count rate saturation is around 10^7 c/s, a factor of 10 above MCPs, and (2) this saturation is typical for one CEM, rather than for "an area," as for MCPs.

For these reasons, we further decide to use 32 CEMs (Figure 2) with a resolution of 1.5° each in azimuth for a total ±24° field of view (FOV). With this design, we can use the full geometric factor of the analyzer, decrease

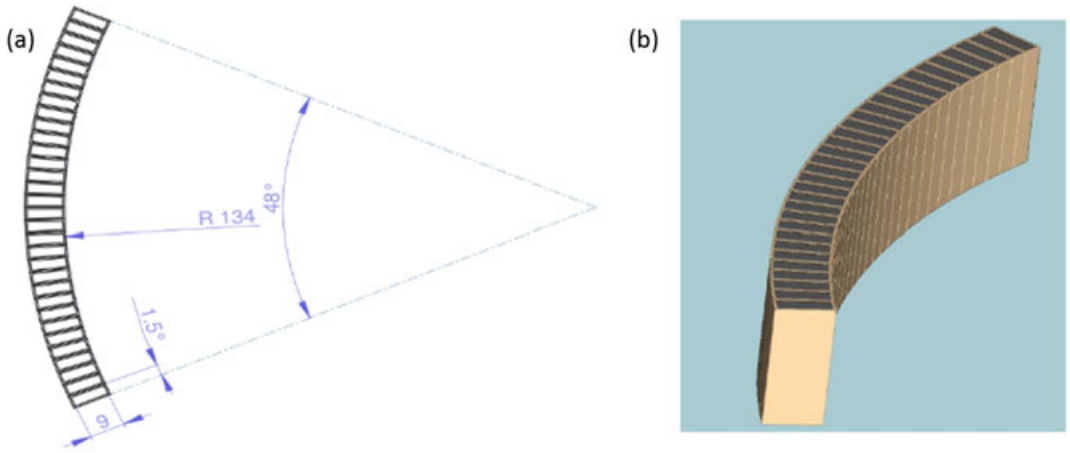

Figure 2. Basic geometry of the CEM detector array that will be used for CSW on THOR. (a) Basic dimensions of the array and (b) its 3-D rendering.

the chance of saturation by a factor of 2, and increase the angular resolution up to 1.5° in azimuth. As demonstrated in section 3, with this design, we will need to perform angular bin summations (2 elevations × 2 azimuths) to increase statistics only in cases of tenuous solar wind. The baseline characteristics of the CSW design, which are further studied in the next sections, are summarized in Table 1.

2.1.2. Analyzer Characterization

The electrostatic analyzer introduced above has been studied in detail through simulations by using two separate software packages (SIMION (http://www.simion.com) and Trace (software developed at Institut de Recherche en Astrophysique et Planétologie (IRAP))) for thorough benchmarking.

These simulations consist in calculating the electrostatic potential around and inside the analyzer mechanical model by using finite differences for SIMION and finite element methods for Trace. A particle beam is launched upstream of the ESA aperture. The particle source used here is a rectangle, uniformly distributed in position, energy, and elevation, while the azimuth for all particles is 0°, as introduced by *Collinson* [2012]. The electrostatic analyzer responses are obtained by studying the energy, elevation, and position of the transmitted particles.

The analyzer energy and elevation responses calculated through simulation are plotted in Figure 3 for an analyzer inner plate voltage of 71.5 V. The two curves show the results with SIMION (red) and Trace (yellow). Both give similar results. The energy response shows that the analyzer constant *K* (which relates the energy band pass to the voltage applied to the analyzer) is 13.8 with an energy resolution of 7%. The elevation response shows a peak in transmission for zero elevation angle with a resolution of about 1.7°. All of these values are in

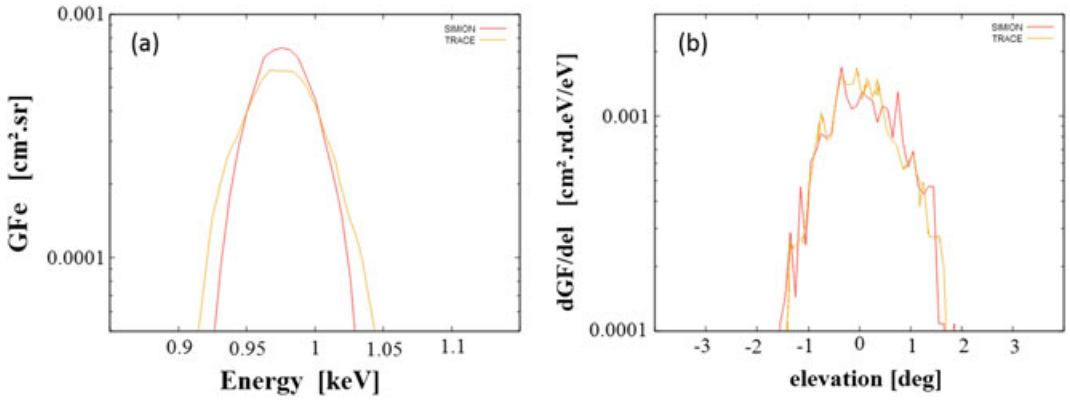

Figure 3. (a) Energy and (b) elevation response obtained with two different codes, SIMION (red) and Trace (yellow).

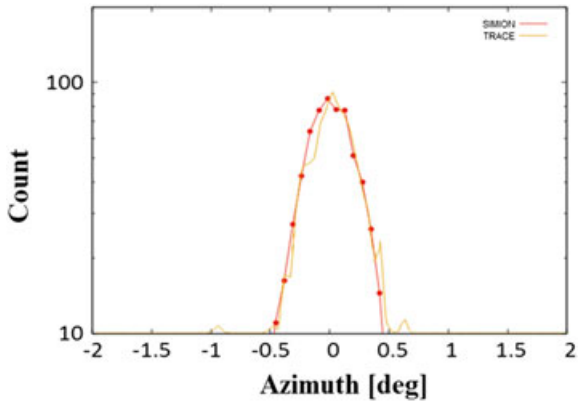

Figure 4. Azimuth analyzer response obtained with two different codes, SIMION (red) and Trace (yellow).

agreement with the scientific requirements of the THOR mission for high angular and energy resolution, as given in Table 1.

The azimuth response is obtained by measuring the angular position of the particles on the detectors, after selection and focusing through the electrostatic analyzer. The results obtained by the two codes for the present ESA characteristics are presented in Figure 4. The simulations show an azimuth angular resolution below 1°, thus well consistent with the scientific requirements as well (cf. Table 1).

2.1.3. Geometric Factor

The last but not the least key parameter that needs to be determined is the analyzer transmission rate or geometric factor (GF). This factor relates the count rate measured to the incident ion energy flux:

$$C_{\text{in}} = \mathbb{GF}_E . J_E \tag{1}$$

This factor is estimated with the method introduced by *Collinson* [2012] (without taking into account the detector efficiency). The formula is given in equation (2), where C_{ijk} is the number of particles which strike the simulated detector, $\Delta Y_b \times \Delta Z_b$ is the rectangle area over which particles are launched, $\overline{E_b}$ and $\overline{\theta_b}$ are the average incident particle energy and elevation, ΔE_b and $\Delta\theta_b$ are the energy and elevation range of the particle source, $\Delta\varphi$ is the angular width of the anodes, E_0 is the peak of the energy acceptance, and N_{in} is the number of incident particles launched. For a 3° azimuthal bin, this factor is about

$$\mathbb{GF}_{3\text{deg}} = \frac{C_{ijk}\ \Delta Y_b\ \Delta Z_b \overline{E_b}\ \Delta E_b\ \Delta\theta_b\ \cos^2\overline{\theta_b}\ \ \Delta\varphi}{E_0^2\ N_{\text{in}}} = 4.4\times 10^{-5}\text{cm}^2\cdot\text{sr}\cdot\text{eV}/\text{eV} \tag{2}$$

This analyzer thus largely responds to the scientific requirements of the THOR mission with an energy resolution around 7%, an elevation resolution below 1.7°, and a resolution in azimuth below 1°. As will be shown later by using actual expected solar wind ion fluxes to estimate the counting statistics, these numbers (and the GF in particular) are also compatible with the proposed increase in elevation and azimuthal angular resolutions to 1.5°.

2.2. Electrostatic Deflection

In addition to the ±24° FOV defined by the 32 CEMs of 1.5° each in the azimuthal plane, the measurement of the 3-D ion distribution function is performed through the use of electrostatic deflectors at the entrance of the analyzer to steer the look direction in the elevation direction as well. This is done by applying appropriate voltages to the deflectors, whose geometry has been optimized to permit an FOV of ±24° in elevation (as for the azimuth FOV). A *D* factor can be defined (*D* in equation (3)). It relates the peak elevation (El) band pass to the deflector voltages ($U_{\text{def}} = Ud_1 - Ud_2$) which define the deflector efficiency:

$$(\text{El} - \text{El}_0) = D\frac{Ud_1 - Ud_2}{E/q} = \frac{D}{K}\frac{Ud_1 - Ud_2}{U_{\text{an}}} = \frac{D}{K}\frac{U_{\text{def}}}{U_{\text{an}}} \tag{3}$$

where *q* is the elementary electron charge and *E* the measured particle energy, which is directly related to the analyzer voltage (U_{an}) through the analyzer constant *K*.

2.2.1. Deflector Design

Designing the deflection system consists of finding the best trade-off between deflection efficiency and elevation band pass. The interdeflector distance defines the elevation range and thus must be large enough to

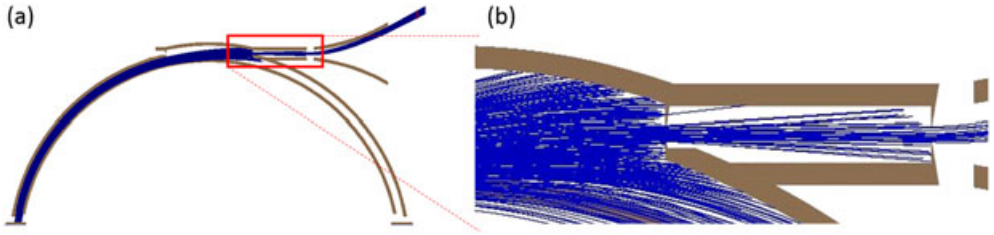

Figure 5. (a) Actual design with sample particle tracing (particles are launched from the detectors on the bottom left) and (b) zoom-in on the collimator area to highlight its importance in determining the elevation of accepted particles, and in turn elevation and energy resolutions.

measure particles within the desired elevation band pass without a decrease in geometric factor (due to mechanical blocking of the particle trajectories). But, on the other hand, to obtain a high efficiency the deflectors must be sufficiently close so as to provide the highest electrostatic field (and thus deflect particles) with minimal applied voltages.

Simulations have been performed to find the minimum interdeflector distance that respects the scientific requirements of the instrument, by calculating the ion trajectories from the detector to the deflectors and determining the associated maximal elevation of the incoming particles. With the design displayed in Figures 1 and 5a, the decrease in geometric factor only appears for elevations around 30°, as discussed later on the basis of Figure 9a. The design is thus appropriate to measure particles within the desired elevation range, with appropriate margins compared to the baseline FOV (±24°). Note that the collimator, which is made of two blade-shaped collimators, also plays a key role in determining the elevation and energy resolutions, as illustrated with particle tracing in Figure 5b.

2.2.2. Deflector Characterization

The first purpose of simulations is to determine the deflector efficiency (through the *D* factor) and thus the maximum voltage to apply between the deflectors to get the required elevation range. The analyzer potential applied here is −71.5 V to select particles with an energy around 1 keV, and deflector voltages are varied. Figure 6 shows the energy-elevation response for different elevations/voltages.

The observed oval shape of the energy-elevation response for no deflection (central plot in Figure 6) corresponds to the typical response of an electrostatic analyzer without deflectors at the entrance. The fact that this transmission function favors slightly higher-energy particles for positive elevations, and conversely lower energy particles for negative elevations, is a classical property of a top-hat analyzer [e.g., *Carlon and McFadden*, 1998]. It merely reflects the fact that given the finite separation of the analyzer hemispheric plates, particles coming from positive elevation can only go through the entire analyzer if they have a slightly higher energy (than the average energy) and radius of curvature. Similarly, only slightly lower energy particles can go through if coming from negative elevations. This fact is illustrated in Figure 7. As can be seen in Figures 6a and 6b, the deflection system exacerbates this effect (oval shape) for negative elevation steering, while it decreases for positive steering. This pure electrostatic optic effect results in a slightly lower angular

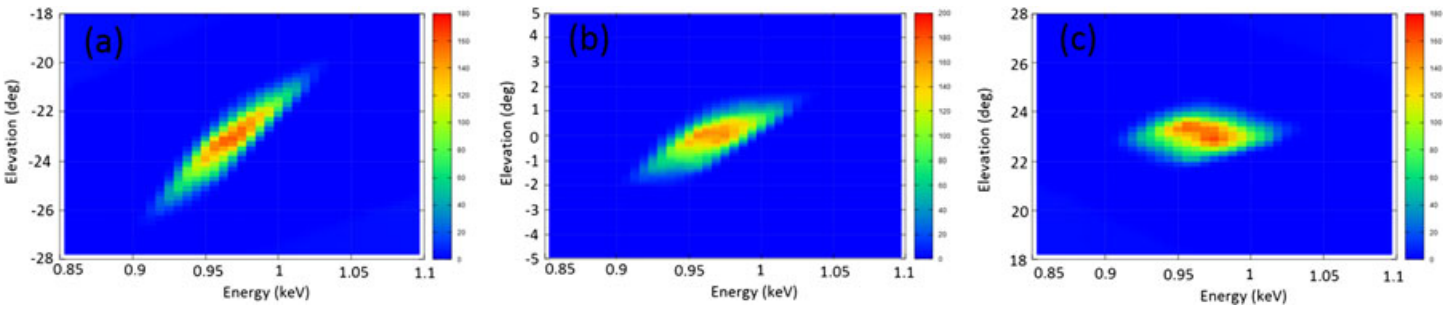

Figure 6. Response function calculated with SIMION showing the transmission rate over the energy and elevation response for three deflector potentials considered: (a) $U_{def} = -170$ V, (b) 0 V, and (c) 170 V. For this simulation both deflectors are polarized in an antisymmetrical fashion.

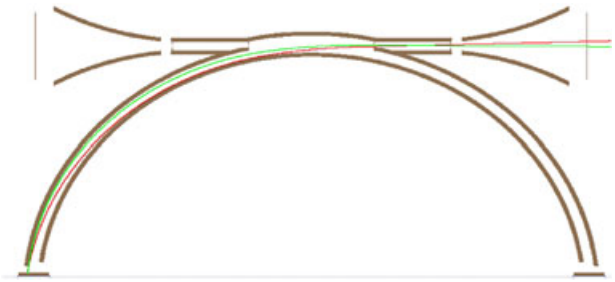

Figure 7. Typical trajectories plotted for two particles: high energy (red) and low energy (green).

resolution for negative elevations (1.7° full width at half maximum as noted previously) but which remains consistent with the science requirements.

Figure 8 illustrates the relation between the deflection angle and the deflector voltage, which can be approximated by a linear function with a constant *D* equal in the present design to 132° ▪ V/V. Therefore, to detect particles with an energy around 20 keV and an elevation of about 25°, the high voltage circuit must provide a voltage of 3.8 kV for the deflectors (or ±1900 V).

2.2.3. Performance Variation With Deflection

Finally, the variation of the analyzer performance with deflection is analyzed. Figure 9 shows the variation of the transmission rate (GF) and analyzer constant *K*. These are constant for all elevations, as required per Liouville's theorem and electrostatic optics. It shows that the deflector geometry is appropriate and no blocking of particle trajectories occurs for the proposed design.

Figure 10 shows the elevation and azimuth responses of this instrument design for different deflector potentials. The center elevation shifts as expected, as a function of the deflector voltage. However, we note a small degradation, as mentioned in section 2.2.2, of the elevation resolution for negative deflections. The azimuth response, on the other hand, shows little variation due to the deflectors, despite a small change in the focal length of the electrostatic analyzer. This is not an issue, however, as we do not want a drastic focusing anyway, in order to mitigate the fact that there is a dead zone between each CEM (~20%). This slight defocusing (yet within ~1° resolution) should indeed permit a smoother response across all CEMs. Despite the slightly degraded elevation resolution at negative elevations, all characteristics satisfy the scientific requirements of the mission.

3. Scientific Performance and Measurement Scheme

The scientific goal of the present design is to measure the full 3-D distribution function of solar wind protons at 1 AU (and alphas, but these are left for future work) in unprecedented details. The objective of this section is to determine the impact of the instrument basic accumulation time and angular resolution (1.5° or 3°) on the statistics of each elementary measurement (counts) given the geometric factor of the proposed design.

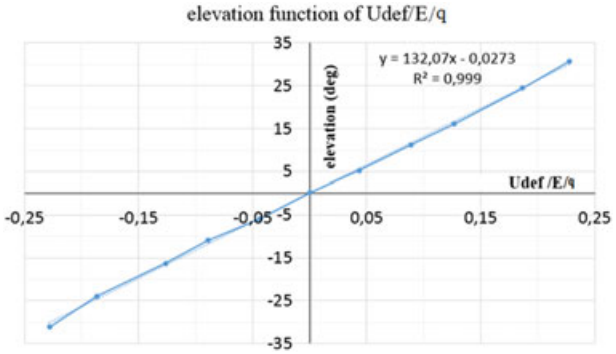

Figure 8. Deflection angle as a function of deflector potentials (per energy per charge).

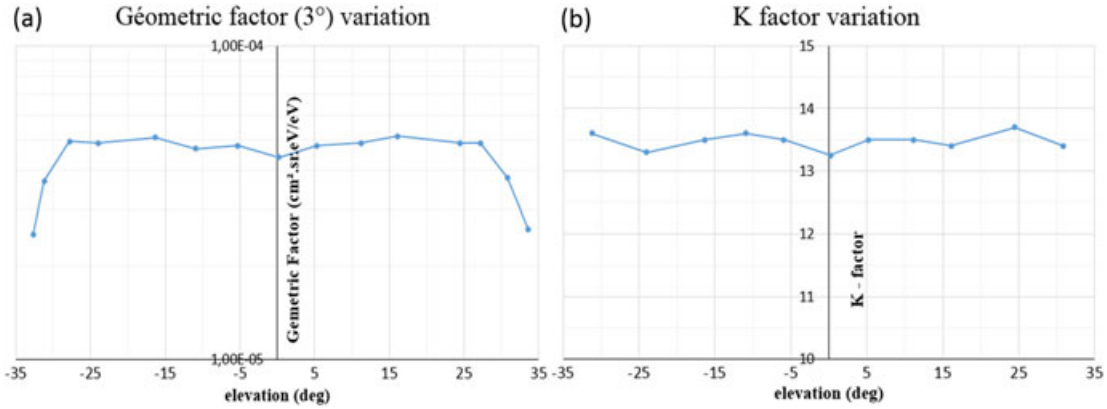

Figure 9. (a) GF and (b) *K*-factor variation as a function of the elevation angle.

3.1. Basic Solar Wind Modeling

As presented in section 2.2, the current design has a GF of 4.4×10^{-5} cm^2 sr eV/eV for 3° resolution in azimuth. However, to ensure that the statistics is sufficient and that the CEM detectors do not saturate, an additional study must be done taking into account known fluxes of solar wind protons at 1 AU. For that purpose, the distribution function of the solar wind proton beam is approximated as a drifting Maxwellian:

$$f(v) = N.\left(\frac{m}{2\pi.k_B.T}\right)^{\frac{3}{2}}.e^{-\left[\frac{v-v_0}{v_{th}}\right]^2}. \quad \text{with } N \text{ the density and } T \text{ the temperature, } v_{th} = \sqrt{\frac{2.kT}{m}} \tag{4}$$

Then the count rate measured by the instrument is related to the distribution function through the geometric factor (with τ as the elementary acquisition time) as follows:

$$C = f\left(\overrightarrow{E}\right).\frac{2\tau.{E_0}^2}{m^2}.\mathbb{GF}_{ijk} = f\left(\overrightarrow{v}\right).\frac{\tau.{v_0}^4}{2}.\mathbb{GF}_{ijk} \tag{5}$$

Figure 11 shows the count rate estimated for different types of solar wind, according to their density, speed, and temperature. Three sets of values are used in Figure 11, with speeds of 400 and 600 km/s and temperatures of 15 and 5 eV, respectively, for the slow and fast solar winds. An unusual case of hot (15 eV) and slow (400 km/s) solar wind is also shown for context. A typical density of 5 cm^{-3} is used in all cases. The maximal count rate for a 3° bin is near 10^7 c/s for a fast solar wind, which is essentially the saturation level of one CEM. By using 32 CEMs over the ±24° FOV, our proposed design thus diminishes this saturation by a factor of 2 and at the same time increases the azimuth angular resolution to 1.5°.

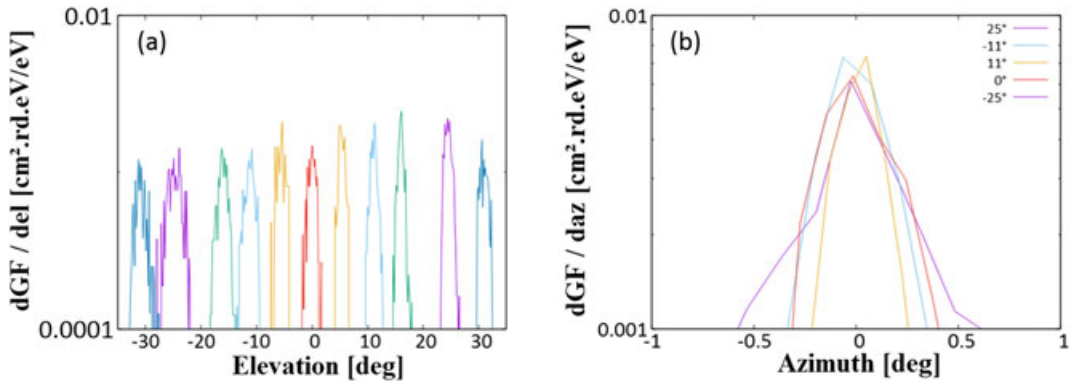

Figure 10. (a) Elevation and (b) azimuth response of the design.

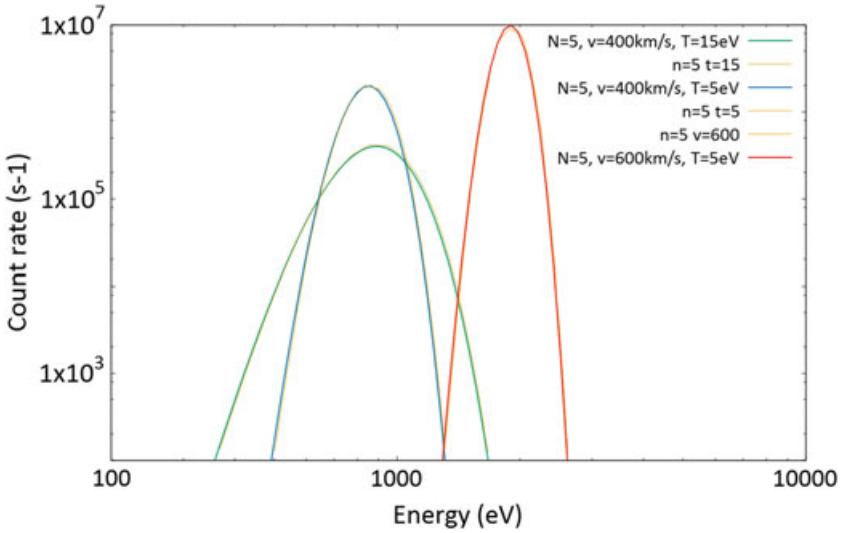

Figure 11. Count rate estimated for a 3° azimuthal angular sector in the present design. There are curves for three types of solar wind: typical slow ($T = 5$ eV and $V = 400$ km/s) and fast ($T = 15$ eV and $V = 600$ km/s) winds, as well as a very unusually hot and slow wind for context ($T = 15$ eV and $V = 400$ km/s). For each type of wind, the count rates have been estimated by using both SIMION and Trace simulations.

3.2. Measurement Scheme

The next aspect of the present study deals with the choice of the energy-elevation stepping scheme and its impact on the accumulated counts measured by the instrument. As mentioned previously, one of the science requirements is to obtain a full 3-D distribution function in 150 ms. This measurement should be done with as many energies and elevations as possible, for science purposes, but this directly impacts the elementary accumulation time and thus the accumulated counts per bin. A trade-off must be found to obtain high time, energy, and angular resolutions, together with a good coverage of the 3-D distribution and a good statistic.

For that purpose the instrument design should use 96 basic energy bins of 7% each over a range of order of 20 eV–20 keV. Because the solar wind is a cold beam of variable peak energy (corresponding to the solar wind bulk speed), a beam tracking strategy will be implemented in order to focus the measurements only on the energy range where significant flux is present (e.g., Figure 11). Several modes will be implemented in order to measure the solar wind beams of variable temperatures, and some modes will be devised in order to measure both protons and alphas (with 16, 24, 32, or 46 energy bins, for instance).

To exemplify the measurement scheme only 16 steps in energy (and 32 elevation) are considered here. The corresponding chronogram is represented in Figure 12. Within each of the 16 steps in energy, the deflector

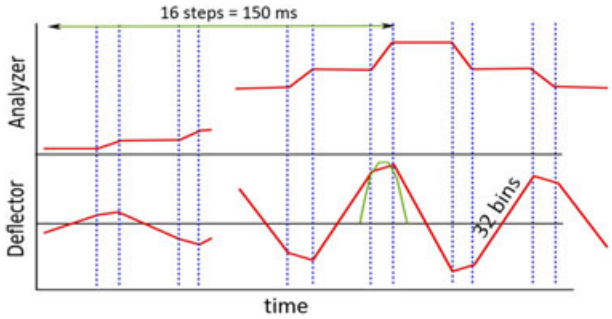

Figure 12. Chronogram with 16 steps in energy and 32 elevation bins. The highest energy step shown after the 150 ms arrow is only meant to show that the next sweep in energy may have a different energy range owing to the requirement for energy tracking of the solar wind proton beam (but this is not discussed in detail in the present paper). Note also that adjacent energy sweeps may be done in successive ascending/descending order so as to avoid dead times required for setting back the high voltages to low values.

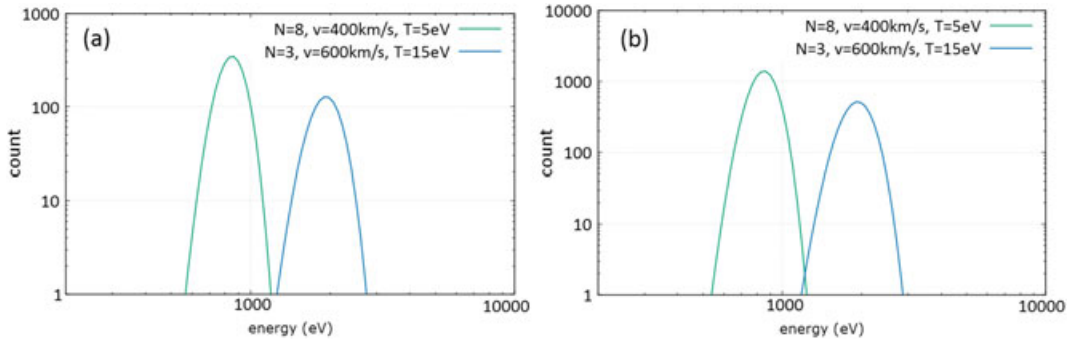

Figure 13. Accumulated counts estimated for a 16 energy step mode with (a) 1.5° and (b) 3° angular bins.

voltages are swept linearly (cf. Figure 8) in order to cover the required elevation range. The full deflection can typically be divided into 16 or 32 basic elevation bins (3° or 1.5°), and appropriate counters are implemented in the FPGA (Field Programmable Gate Arrays) by using the baseline accumulation time.

3.3. Detailed Scientific Performance

The statistic is given by the accumulated counts:

$$C_{\text{acqu}} = f\left(\vec{E}\right).\frac{2.{E_0}^2}{m^2}.\ \mathbb{GF}_{ijk}.\ \frac{T_{3\text{-D}}}{n_{\text{step}_E}.\ n_{\text{step}_{\text{el}}}} \tag{6}$$

The counts that would be observed as a function of energy with the present instrument design are displayed in Figure 13 for two angular resolutions and solar wind properties (slow and fast solar winds). Figure 13a shows the counts expected for 16 steps in energy and the highest angular resolution (32 elevations and azimuths of 1.5° each). As can be seen, the statistics is reasonably high for such typical solar wind densities. In cases of tenuous solar wind (e.g., 1 cm^{-3}), the statistics can be increased by a factor of 4 by summing angular bins 2×2 so that the distribution function is now made up of 16 elevations and azimuths of 3° each. The statistics obtained by such a summation process is illustrated in Figure 13b. This measurement scheme can easily be adapted to accomodate higher or lower temporal resolutions, pending further analysis in phase A and later.

The unprecedented high-resolution measurements that are expected from this design are illustrated in Figure 14. Figure 14a shows the proton velocity distribution from a hybrid Vlasov-Maxwell simulation [*Valentini et al*., 2007] of solar wind turbulence [*Servidio et al*., 2012, 2015; *Valentini et al*., 2014], displaying a complex structure in velocity space with the presence of a marked particle beam. The corresponding observations expected for the present design (THOR CSW) and the PAS instrument on Solar Orbiter are respectively shown in Figures 14b and 14c (here the solar wind bulk speed is 500 km/s). This figure highlights the

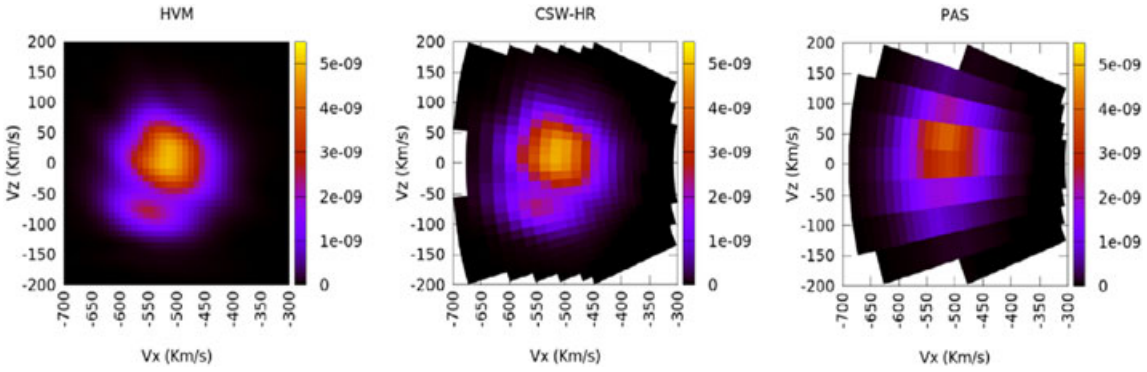

Figure 14. Illustration of the expected measurements of the proton distribution function on the basis of solar wind simulations described in *DeMarco et al*. [2016], respectively for the properties of (a) the simulation itself [*Valentini et al*., 2007], (b) the present design (THOR CSW instrument), and (c) the Solar Orbiter PAS instrument. The data are represented in a system equivalent to geocentric solar equatorial coordinates.

capability of this design to isolate fine structures in the distribution function such as faint suprathermal beams [cf. also *DeMarco et al.*, 2016].

3.4. Additional Comments

The proposed measurement scheme leads to high constraints for the electronic system of CSW. For instance, the slew rate of the deflector power supplies must be higher than 500 V/ms to measure the 2-D distribution of a 20 keV particle within about 8 ms (cf. Figure 12), but this is achievable with current HV systems. The front-end electronics also is a key for instrument performance. The electronic front-end must be able to detect particles with a count rate close to CEM saturation (~10^7 c/s). For that purpose, a multichannel application-specific integrated circuit is currently being designed. The FPGA counters must also be efficient enough to register all counts from the front-end.

Finally, the amount of data resulting from such a high resolution (time, energy, and angle) measurement scheme is very large (~1800 kbit/s or more). Although the instrument will be continuously operating in burst mode, the telemetry is not sufficient to downlink all data in burst. Burst data will thus only be downlinked in selected locations by using a "Scientist In The Loop" system akin to that used for the Magnetospheric Multiscale (MMS) mission [*Baker et al.*, 2016; *Fuselier et al.*, 2016; *Phan et al.*, 2016]. All these additional aspects are currently being studied and will be reported in future communications.

4. Conclusions

This paper described an instrument design that permits unprecedentedly accurate measurements of the solar wind proton beam with high temporal, energy, and angular resolutions. These properties fulfill the requirements of the THOR mission, which aims at addressing collisionless turbulence in space plasmas. We first described the mechanical design of the proposed instrument. It is composed of a top-hat electrostatic analyzer for incident particle energy-per-charge selection, a collimator at its entrance for obtaining the appropriate high energy resolution, as well as deflectors for the elevation angle selection. A first analysis showed that microchannel plates (MCPs) cannot be used because of their low count rate saturation. Instead, channel electron multipliers (CEMs) were chosen. Simulations were performed to define an appropriate electrostatic analyzer. It was designed to have an analyzer constant K of 13.8, an energy resolution of 7%, an elevation resolution of 1.7°, and a transmission rate (geometric factor) of $4.4 \times 10^{-5} \mathrm{cm}^2 \cdot \mathrm{sr} \cdot \mathrm{eV/eV}$ for 3° azimuthal bins. Deflectors were also designed through simulations to optimize the applied voltages, FOV, and angular resolution. The simulations show a deflector efficiency of 132° ▪ V/V for an elevation range larger than ±25°, thus fulfilling the FOV requirements. Finally, the CSW response has been studied for typical solar wind conditions assuming Maxwellian distribution functions. With the proposed design, the count rate is about 10^7 c/s. This is consistent with the choice of CEMs as detectors, instead of MCPs, to avoid saturation. To further decrease the chance of saturation and at the same time increase the angular resolution by a factor of 2, we decided to design the instrument with 32 CEMs covering 1.5° each over the ±24° azimuthal FOV. In summary, thanks to its high geometric factor and 32 CEMs, this design will provide the THOR CSW instrument with unprecedentedly fast (150 ms) and high angular (1.5°) resolution measurements of the solar wind protons and alphas. A direct comparison with realistic simulations of turbulent plasmas reveals that the proposed instrumentation will be crucial for the description of the fine dynamics of the solar wind.

Acknowledgments

The simulations were performed by using the SIMION software, available at http://simion.com/. The simulations' input and output data (available in the most part in the tables and figures provided) can be obtained by contacting the authors (acara@irap.omp.eu or blavraud@irap.omp.eu). Work at IRAP was supported by CNRS and CNES. We also acknowledge support from the SME EREMS in Flourens, France. Work at IASB-BIRA was supported by PRODEX THOR-CSW Development PEA 4000116805. Work at University of Calabria, Italy, and at IAPS/INAF, Rome, has been supported by the Agenzia Spaziale Italiana under the contract ASI-INAF 2015-039-R.O. "Missione M4 di ESA: Partecipazione Italiana alla fase di assessment della missione THOR."

References

Baker, D. N., L. Riesberg, C. K. Pankratz, R. S. Panneton, B. L. Giles, F. D. Wilder, and R. E. Ergun (2016), Magnetospheric multiscale instrument suite operations and data system, *Space Sci. Rev.*, *199*(1–4), 545–575, doi:10.1007/s11214-014-0128-5.

Bruno, R., and V. Carbone (2013), The solar wind as a turbulence laboratory, *Living Rev. Solar Phys.*, *10*, 2, doi:10.12942/lrsp-2013-2.

Carlon, C. W., and J. P. McFadden (1998), *Design and Application of Imaging Plasma Instruments, Measurement Techniques in Space Plasmas: Particles*, *Geophys. Monogr.*, vol. 102, AGU, Washington D. C.

Carlson, C. W., et al. (1982), An instrument for rapidly measuring plasma distribution functions with high resolution, *Adv. Space Res.*, *2*(7), 67–70, doi:10.1016/0273-1177(82)90151-X.

Collinson, G. A. (2012), The geometric factor of electrostatic plasma analyzers: A case study from the Fast Plasma Investigation for the Magnetospheric Multiscale mission, *Rev. Sci. Instrum.*, *83*, 033303, doi:10.1063/1.3687021.

DeMarco, R., M. F. Marcucci, R. Bruno, R. D'Amicis, S. Servidio, F. Valentini, B. Lavraud, P. Louarn, and M. Salatti (2016), Importance of energy and angular resolutions in top-hat electrostatic analysers for solar wind proton measurements, *J. Instrum.*, *11*(08C08010).

Fuselier, S. A., W. S. Lewis, C. Schiff, R. Ergun, J. L. Burch, S. M. Petrinec, and K. J. Trattner (2016), Magnetospheric multiscale science mission profile and operations, *Space Sci. Rev.*, *199*(1–4), 77–103, doi:10.1007/s11214-014-0087-x.

Kasper, J. C., et al. (2016), Solar Wind Electrons Alphas and Protons (SWEAP) investigation: Design of the solar wind and coronal plasma instrument suite for Solar Probe Plus, *Space Sci. Rev.*, *204*(1), 131–186, doi:10.1007/s11214-015-0206-3.

Lin, R. P., et al. (1995), A three-dimensional plasma and energetic particle investigation for the wind spacecraft, *Space Sci. Rev.*, *71*(1), 125–153, doi:10.1007/BF00751328.

Marsch, E. (2006), Kinetic physics of the solar corona and solar wind, *Living Rev. Solar Phys.*, *3*, 1, doi:10.12942/lrsp-2006-1.

McComas, D. J., S. J. Bame, P. Barker, W. C. Feldman, J. L. Phillips, P. Riley, and J. W. Griffee (1998), Solar Wind Electron Proton Alpha Monitor (SWEPAM) for the Advanced Composition Explorer, *Space Sci. Rev.*, *86*(1), 563–612, doi:10.1023/A:1005040232597.

Montgomery, M. D., S. P. Gary, D. W. Forslund, and W. C. Feldman (1975), Electromagnetic ion-beam instabilities in the solar wind, *Phys. Rev. Lett.*, *35*, 667–670, doi:10.1103/PhysRevLett.35.667.

Ogilvie, K. W., et al. (1995), SWE, a comprehensive plasma instrument for the WIND spacecraft, *Space Sci. Rev.*, *71*, 55–77, doi:10.1007/BF00751326.

Phan, T. D., M. A. Shay, J. P. Eastwood, V. Angelopoulos, M. Oieroset, M. Oka, and M. Fujimoto (2016), Establishing the context for reconnection diffusion region encounters and strategies for the capture and transmission of diffusion region burst data by MMS, *Space Sci. Rev.*, *199*(1–4), 631–650, doi:10.1007/s11214-015-0150-2.

Pollock, C., et al. (2016), Fast plasma investigation for magnetospheric multiscale, *Space Sci. Rev.*, doi:10.1007/s11214-016-0245-4.

Rème, H., et al. (2001), First multispacecraft ion measurements in and near the Earth's magnetosphere with the identical Cluster Ion Spectrometry (CIS) experiment, *Ann. Geophys.*, *19*(10–12), 1303–1354, doi:10.5194/angeo-19-1303-2001.

Schwartz, S. J., et al. (2009), Cross-scale: Multi-scale coupling in space plasmas, *Exp. Astr.*, *23*, 1001–1015, doi:10.1007/s10686-008-9085-x.

Servidio, S., F. Valentini, F. Califano, and P. Veltri (2012), Local kinetic effects in two-dimensional plasma turbulence, *Phys. Rev. Lett.*, *108*, 045001, doi:10.1103/PhysRevLett.108.045001.

Servidio, S., F. Valentini, D. Perrone, A. Greco, F. Califano, W. H. Matthaeus, and P. Veltri (2015), A kinetic model of plasma turbulence, *J. Plasma Phys.*, *81*, 325810107, doi:10.1017/S0022377814000841.

Vaivads, A., et al. (2016), Turbulence Heating ObserveR—Satellite mission proposal, *J. Plasma Phys.*, *82*, 5, doi:10.1017/S0022377816000775.

Valentini, F., P. Travnicek, F. Califano, P. Hellinger, and A. Mangeney (2007), A hybrid-Vlasov model based on the current advance method for the simulation of collisionless magnetized plasma, *J. Comput. Phys.*, *225*, 753, doi:10.1016/j.jcp.2007.01.001.

Valentini, F., S. Servidio, D. Perrone, F. Califano, W. H. Matthaeus, and P. Veltri (2014), Hybrid Vlasov-Maxwell simulations of two-dimensional turbulence in plasmas, *Phys. Plasmas*, *21*, 082307, doi:10.1063/1.4893301.